Inter-comparison and evaluation of Arctic sea ice type products

Yufang Ye, Yanbing Luo, Yan Sun, Mohammed Shokr, Signe Aaboe, Fanny Girard-Ardhuin, Fengming Hui, Xiao Cheng, Zhuoqi Chen

https://doi.org/10.5194/tc-2022-95
Preprint. Discussion started: 19 May 2022

The Cryosphere Discussions

Inter-comparison and evaluation of Arctic sea ice type products

Yufang Ye[1], Yanbing Luo[1], Yan Sun[1], Mohammed Shokr[2], Signe Aaboe[3], Fanny Girard-Ardhuin[4], Fengming Hui[1], Xiao Cheng[1] and Zhuoqi Chen[1]

[1]School of Geospatial Engineering and Science, Sun Yat-sen University, and Southern Marine Science and Engineering Guangdong Laboratory (Zhuhai), Zhuhai 519082, China
[2]Meteorological Research Division, Environment and Climate Change Canada, Toronto M3H5T4, Canada
[3]Department of Remote Sensing and Data Management, Norwegian Meteorological Institute, Tromso, Norway
[4]Laboratoire d'Océanographie Physique et Spatiale (LOPS), Ifremer-Univ. Brest-CNRS-IRD, IUEM, F-29280, Plouzané, France

Correspondence to: Zhuoqi Chen (chenzhq67@mail.sysu.edu.cn)

Abstract. Arctic sea ice type (SIT) variation is a sensitive indicator of climate change. However, systematic inter-comparison and analysis for SIT products are lacking. This study analyzed nine SIT products from five SIT retrieval approaches covering the winters from 1999 to 2018. These SIT products were inter-compared towards sea ice age product and evaluated with Synthetic Aperture Radar images. Among all, the largest daily Arctic multiyear ice (MYI) extent difference reaches 4.5×10^6 km^2, while that in monthly data varies between 0.6×10^3 km^2 and 3.6×10^6 km^2. Overall speaking, the Zhang- and KNMI-SIT products based on Ku-band scatterometer perform the best. However, when using C-band scatterometer, KNMI-SIT shows overestimation of MYI in the early winter, and Zhang-SIT shows underestimation with anomalous fluctuations. C3S- and OSISAF-SIT show large daily variability. IFREMER-SIT generally underestimates MYI. Factors that could impact their performances are analyzed and summarized: (1) Ku-band scatterometer generally performs better than C-band scatterometer on SIT discrimination, while the latter sometimes identifies first-year ice (FYI) more accurately, especially when FYI and MYI are highly mixed. (2) Simple combination of scatterometer and radiometer data is not always beneficial, e.g. under circumstances with strong atmospheric influence on microwave signatures. (3) The representativeness of training data and efficiency of classification are crucial for SIT classification. Spatial and temporal variation of characteristic training dataset should be well accounted in the SIT method. Additionally, the change of separation pattern of microwave data could influence the adaptive classification method. (4) Post-processing corrections play important roles and should be considered with caution.

1 Introduction

Sea ice is an important component of the earth system and at the same time a sensitive indicator of climate change. Its area has decreased dramatically in the Arctic over the past four decades (Comiso, Parkinson, et al. 2008, Onarheim, Eldevik, et al. 2018). The average ice thickness and volume decreased significantly during the last decades (Kwok and Cunningham 2015, Liu, Key, et al. 2020, Petty, Kurtz, et al. 2020). Meanwhile, the ice drifting and deformation rates are increasing (Hakkinen, Proshutinsky, et al. 2008, Kwok, Spreen, et al. 2013). The Arctic sea ice has been increasingly dominated by thin and young

https://doi.org/10.5194/tc-2022-95
Preprint. Discussion started: 19 May 2022

first-year ice (FYI) instead of thick and firm multiyear ice (MYI), the ice that has survived at least one summer melt (Maslanik, Fowler, et al. 2007). FYI comprised 35-50% of the ice cover in the mid-1980s. In comparison, this proportion increased to ~70% in 2019, while MYI covered less than one third of the Arctic Ocean (Kwok 2018, Perovich, Meier, et al. 2019). The change of sea ice type (SIT) distribution impacts the climate of the Arctic and mid-high latitude regions through different thermodynamic and dynamic processes (Liu, Curry, et al. 2012, Screen, Simmonds, et al. 2013, Boisvert, Petty, et al. 2016, Belter, Krumpen, et al. 2021), which further influences the Arctic ecosystem and the commercial maritime activities (Emmerson and Lahn 2012, Meier, Hovelsrud, et al. 2014). Previous studies found that the MYI area anomalies can largely explain (about 85%) the variance in Arctic sea ice volume anomalies (Kwok, 2018). Understanding the distribution and transition of Arctic SIT (especially MYI) is therefore of great scientific and practical importance.

To monitor Arctic sea ice type distribution changes at hemispheric scale, various algorithms have been developed using microwave satellite data. These algorithms identify SIT based on the distinctive radiometric and scattering characteristics of sea ice. Passive microwave observations, brightness temperatures (Tb) from radiometer, have been commonly utilized to monitor the evolution of Arctic MYI (Lomax, Lubin, et al. 1995, Comiso 2012, Ye and Heygster 2015, Lee, Sohn, et al. 2017). For active microwave (scatterometer) data, Kwok et al. successively used fixed thresholds on backscatter coefficient (σ^0) from QuikSCAT (QSACT) and Advanced Scatterometer (ASCAT) data to obtain daily MYI coverages spanning from 1999 to 2017 (2018). By comparing the MYI area changes to MYI export from Fram Strait during winter, the uncertainty was found to be of ±10% in area coverage within near even mixtures of MYI and seasonal ice (Kwok 2004). Another long-term SIT distribution record since 1992 was derived based on geophysical module functions and double fixed thresholds from inter-calibrated scatterometer data (from European Remote Sensing (ERS), QSCAT and ASCAT) (Belmonte Rivas, Otosaka, et al. 2018). Time-dependent dynamic threshold was applied for ice type classification from 2002 to 2009 using QSCAT data (Swan and Long 2012), and extended to 2014 with Oceansat-2 Ku-band Scatterometer (OSCAT) (Lindell and Long 2016). Researchers found the classifier accuracy can be improved by combining radiometer and scatterometer data (Yu, Clausi, et al. 2009). Multi-sensor approaches have been applied to derive SIT products (Shokr, Lambe, et al. 2008, Lindell and Long 2016, Zhang, Yu, et al. 2019). Although the performances of passive and active microwave data on ice classification under various conditions have been compared in several studies (Yu, Clausi, et al. 2009, Rivas, Otosaka, et al. 2018, Zhang, Yu, et al. 2021), there is rarely analysis for ergodic combination use of both data.

Comparison and evaluation of SIT products are needed for error estimation, error source control and improvement of SIT retrieval methods. Lacking of in-situ data, evaluations of most SIT algorithms and products are limited to indirect validation. Consistency with other sea ice products is regarded as one of the best approaches (Belmonte Rivas, Otosaka, et al. 2018). Operational SIT maps, ice charts, buoy measurements and limited ship observations are commonly used (Lee, Sohn, et al. 2017, Zhang, Yu, et al. 2019). While ice chart is used as “ground truth” in some validation (Aaboe, Breivik, et al. 2016), some MYI classifications correspond to a MYI concentration of approximately 50% or greater in the ice charts (Lindell and Long 2016), indicating the overestimation of MYI in ice charts. Synthetic aperture radar (SAR) images are also used to evaluate ice

https://doi.org/10.5194/tc-2022-95
Preprint. Discussion started: 19 May 2022

type classification accuracy. The inconsistencies between products are attributed to the usage of different thresholds and satellite observation inputs (Ezraty and Cavanié 1999, Belmonte Rivas, Verspeek, et al. 2012). To date, systematic inter-comparison and method analysis for SIT products are still lacking. The questions remain as to how the operational SIT products perform, how we choose SIT product for different applications, and what factors we should consider to improve the SIT products?

This study aims to investigate differences among SIT products and give comprehensive evaluations. We inter-compared nine SIT products from five SIT retrieval approaches for winters from 1999 to 2018 in this paper. Spatio-temporal variations and retrieval methods of the SIT products are detailed investigated. This paper is organized as follows. Section 2 introduces the SIT products and ancillary datasets. Section 3 starts with temporal and spatial analysis of the SIT products, and proceeds with regional validation with SAR images. Factors that influence the performance of SIT products are discussed in Section 4. Finally, conclusions are highlighted in Section 5.

2 Data

2.1 Sea ice type product

This study inter-compares five series of SIT products from 1999 to 2018, including SIT products obtained from the Copernicus Climate Change Service (referred to as C3S-SIT) (Aaboe, Sørensen, et al. 2021), the Ocean and Sea Ice Satellite Application Facility (referred to as OSISAF-SIT) (Breivik, Eastwood, et al. 2012, Aaboe, Breivik, et al. 2014), the Royal Netherlands Meteorological Institute (KNMI) (referred to as KNMI-SIT) (Rivas, Otosaka, et al. 2018), CERSAT/Ifremer (referred to as IFREMER-SIT) (Girard-Ardhuin 2016), and Beijing Normal University (referred to as Zhang-SIT) (Zhang, Yu, et al. 2019). Microwave radiometer and scatterometer are used to discriminate MYI and FYI due to their distinctive signatures. However, the radiometric and scattering signatures of MYI and FYI become indistinguishable when it comes to the melting season, when microwave radiation can only penetrate the top layer of melting snow (Carsey 1985, Hallikainen and Winebrenner 1992, Kern, Rösel, et al. 2016). As a result, most SIT products only provide data of the winter months (mostly from October to April, some even from November to April). Basic information of the SIT products is shown in Table 1, with time line of satellite inputs visualized in Fig. 1. Among all, C3S-SIT and the OSISAF-SIT before 2010 solely use microwave radiometer data, while KNMI- and IFREMER-SIT only use scatterometer data. For Zhang-SIT and the OSISAF-SIT since 2010, both radiometer and scatterometer measurements are utilized.

C3S-SIT (within the time period of this study) is based on coarse resolution radiometer data of the Special Sensor Microwave/Imager (SSM/I) and followed by the Special Sensor Microwave Image/Sounder (SSMIS), aboard the Defense Meteorological Satellite Program with multi-frequency Tb measurements. The Tb measurements are corrected by auxiliary data including sea ice concentration and atmosphere reanalysis data and a Radiative Transfer Model function (Wentz 1997). C3S-SIT uses a Bayesian approach to discriminate open ocean and sea ice. The spectral Gradient Ratio between vertical

https://doi.org/10.5194/tc-2022-95
Preprint. Discussion started: 19 May 2022

polarized channels of 37GHz and 19GHz (GR_{37v19v}) is used for further ice type classification. The probability density functions (PDFs) of given ice classes used in the Bayesian classification are dynamically derived from training datasets, which are extracted from fixed target areas during 15-day period centered on the specific day (Aaboe, Sørensen, et al. 2018). Within the C3S-SIT framework, the first major version (referred to as C3S-1) was produced as climate-consistent data records based on long-time satellite data input. In 2021, a second major version (referred to as C3S-2) is released, in which the main upgrades include the primary input satellite data, the reanalysis data used in atmospheric correction of Tbs and the implementation of a temperature-based correction scheme.

OSISAF-SIT is a near-real time product which uses a similar method as C3S-SIT, with atmospheric correction and a Bayesian approach. It has been running operational since 2005 with several upgrades up until today. Initially, it was running as a single sensor product based on only SSM/I (later replaced by SSMIS) but since 2010 it became a multi-sensor product by introducing scatterometer data. Since 2016, the medium-resolution radiometer, Advanced Microwave Scanning Radiometer 2 (AMSR-2) replaced SSMIS as the primary passive microwave radiometer. Advanced Microwave Scanning Radiometer for EOS (AMSR-E) aboard Aqua satellite is a twelve-channel, six-frequency passive microwave radiometer, which was launched in 2002 and stopped functioning in 2011. As its successor, AMSR-2 has been working since 2012. AMSR-E/2 has higher spatial resolution compared to SSMI/SSMIS. Scatterometer data comes from ASCAT on EUMETSAT's Metop-A since 2010, including Metop-B since 2016, and Metop-C since 2020. The algorithm makes use of daily updated training dataset and PDFs since 2015. Before 2015 static PDFs were used instead. Sea ice class-probabilities are estimated for GR_{19v37v} and σ^0 on swath projection at first. Then the fusion of radiometer and scatterometer is performed by gridding swath results with given weights. Both C3S- and OSISAF-SIT provide an ambiguous class (where the composition could be either pure FYI, pure MYI or the mixture, referred to as Amb), and the products are provided with processing flags and uncertainty fields.

KNMI-SIT is purely based on scatterometer data, including QSCAT, OSCAT and ASCAT data (corresponding SIT products referred to as KNMI-Q, KNMI-O, and KNMI-A, respectively). QSCAT is a Ku-band (13.4 GHz) conically scanning pencil-beam scatterometer. The inner beam is horizontally polarized (HH) at an incidence angle of 46°, whereas the outer beam is vertically polarized (VV) at an incidence angle of 54°. OSCAT is similar to QSCAT, operating at the frequency of 13.5 GHz with incidence angle for inner HH beam at 49° and outer VV beam at 57°. ASCAT is a C-band (5.255 GHz) scatterometer with 3 vertically polarized (VV) antennas, whose incidence angle varies between 25° and 65°. KNMI-SIT uses a refined Bayesian algorithm based on the probabilistic distances to the Geophysical Model Functions of ocean wind and sea ice. Fixed thresholds extracted from stable wintertime (March) data are adopted for sea ice type classification. In KNMI-SIT, MYI is classified into Second Year ice (SYI) and older MYI, which could be regarded as qualitative proxy sea ice age/thickness (Early and Long 1997, Belmonte Rivas, Otosaka, et al. 2018). In this study, backscatter data from OSCAT is not utilized by other series of SIT products. Inter-comparison and evaluation mainly concern KNMI-Q and -A.

IFREMER-SIT is another scatterometer-only product. It uses QSCAT and ASCAT data for the years of 1999-2015, referred to as IFREMER-Q and IFREMER-A, respectively. In IFREMER-A, backscatter coefficients from ASCAT are normalized to

https://doi.org/10.5194/tc-2022-95
Preprint. Discussion started: 19 May 2022

the backscatter at a constant incidence angle of 40° and resampled to a polar stereographic grid of 12.5 km. In IFREMER-SIT, a series of time-varying thresholds are used for the separation between MYI and FYI. These thresholds are derived by analyzing the backscatter data for several winters and are found to be seasonally consistent (Girard-Ardhuin 2016).

Zhang-SIT employs adaptive classification method based on the thought of clustering, using radiometer and scatterometer data. The radiometer data are utilized in a way that AMSR-E/2 data comes prioritized whenever available and are replaced with SSMIS whenever missing. Scatterometer data is obtained from QSCAT and ASCAT successively since QSCAT stopped functioning. Meanwhile, scatterometer data was enhanced to the spatial resolution of 4.45 km by the scatterometer image reconstruction technique (Long, Hardin, et al. 1993, Early and Long 2001). Correction methods based on sea ice motion and spatial consistency are used for result improvement (Zhang, Yu, et al. 2019).

Among all the SIT products presented here, OSISAF-SIT is a near-real-time SIT product (5-hour latency) for operational applications. The retrieval scheme and satellite data used for this product are upgraded on regular basis and as being a near-real-time operational product, no effort is done to reprocess the archive data. Compared with climate consistent data record SIT products, near-real-time operational product is thus not recommended for climate research. However, for systematic inter-comparison and evaluation of different SIT retrieval schemes, both kinds of SIT products are included in this study.

2.2 Other data

In this study, sea ice age (SIA) product and SAR images were used for inter-comparison and evaluation, respectively. In addition, sea ice drift product and atmosphere reanalysis data were utilized to provide additional information for ice type identification.

The SIA product is from the National Snow and Ice Data Center, referred to as NSIDC-SIA. This product is derived by tracking ice trajectories, using passive and active microwave observations, as well as auxiliary data such as drifting buoys. It is generated from tracking of virtual Lagrangian ice parcels of each grid cell (Fowler, Emery, et al. 2004), limited by the simple drift model and the oldest ice age assignment of grids (Korosov, Rampal, et al. 2018). NSIDC-SIA is available in standardized Equal-Area Scalable Earth (EASE) grid with 12.5 km spacing for the whole year with weekly resolution from 1984 to 2020. For comparison, grid cells with ice age older than one year are regarded as MYI.

Radarsat-1 (referred to as RS-1) and Sentinel-1 SAR images were both used for validation. RS-1 operated from 1995 to 2013, with SAR instrument working at the frequency of 5.3 GHz (C-band) and polarization of HH. The incidence angle ranges from 20° to 49°. Sentinel-1 has been in orbit since 2014. It is a SAR mission, providing cross-polarized (HV or HH) images at the frequency of 5.4 GHz, with incidence angle ranging from 18.9° to 47.0°. Images from Radarset-1 are achieved in Scanning SAR Wide B Mode. Those from Sentinel-1 are in Extra-Wide swath Mode. Images are radiometrically calibrated and projected to UTM projection with pixel size of 50 m for Radarsat-1 data and 160 m for Sentinel-1 data respectively. A refined thermal noise removal method is used to pre-process Sentinel-1 images (Sun and Li 2021). **Fig. 2** shows the geolocations and acquiring dates of the SAR images.

https://doi.org/10.5194/tc-2022-95
Preprint. Discussion started: 19 May 2022

For better interpretation of SAR images, auxiliary data such as ice drift product and atmospheric reanalysis data were used in the validation session. The 3-daily Merged drift product from CERSAT/Ifremer is derived from QSCAT (or ASCAT since 2009) backscatter and SSM/I Tb fields (Girard-Ardhuin and Ezraty 2012). Reanalysis data including 2-m air temperature and 10-m wind is from ERA5 hourly dataset, produced using 4D-Var data assimilation and model forecasts in CY41R2 of the European Centre for Medium-Range Weather Forecasts integrated Forecast System (ECMWFs) (Hersbach, Bell, et al. 2018).

3 Result

This section starts with a temporal and spatial comparison of the SIT products. It then proceeds with validation against SAR images. The temporal and spatial comparison provides clues of the overall performance, while the evaluation against SAR images provides more concrete evidence in a case study of five representative cases.

All the comparisons were performed on the pre-defined area within the Arctic Basin and limited by the polar hole of 87°N, outline of which is as delineated by the red contour in **Fig. 2**. For analysis of spatial patterns, the area is divided into three regions: the central Arctic Ocean (CAO), the East Siberian Sea (ESS) and the Barents Sea (BS). Different SIT distribution patterns are found in the three regions.

3.1 Temporal analysis

SIT products depict the distribution of MYI and FYI. Temporal analysis in this section focuses on the MYI extent. For SIT products, MYI extent is estimated as the integral of all pixels specified as multiyear sea ice within studied area. Note that both SYI and MYI (ice that is older than two years here) classes in KNMI-SIT are included in the calculation of MYI extent. The Amb class in C3S- and OSISAF-SIT could be regarded as MYI and FYI thus the MYI extent is calculated under both circumstances, resulting in a value for the classified MYI and an upper value including the ambiguous class as well for each product (shaded time series in Fig. 3, 4 and 5). For NSIDC-SIA, extent is calculated by general extent of pixels with corresponding age. Data deficiency area around the North Pole of SIT products is excluded from extent calculation and analysis.

3.1.1 Daily MYI extent variation

Daily MYI extent from the nine SIT products were compared with the NSIDC-SIA product for winters from 1999 to 2018 (Fig. 3). Theoretically, since FYI can only turn to MYI when surviving a melting season, there should be a decreasing trend of MYI extent within the winter when considering the entire Arctic sea ice. The MYI extent can temporarily or regional increase due to the divergent movements (Kwok, Cunningham, et al. 1999).

The SIT products show overall decreasing trend of MYI extent through most of the winters as expected. Exceptions are found in some of the winters. For instance, Zhang-SIT shows near constant MYI extent in the winters of 2007-2008 and 2009-2010. C3S-SIT and OSISAF-SIT exhibit increasing MYI extent in the second half of winter 2016-2017, and other years the SIT

https://doi.org/10.5194/tc-2022-95
Preprint. Discussion started: 19 May 2022

show increasing extent in the first half of the winter like 2004-2005 for the C3S-SITs and 2009-2010 for OSISAF-SIT. KNMI-A presents dramatic peaks all years in the first half of the winter.

In comparison, KNMI-SITs have overall the highest MYI extent values especially KNMI-A (C-band). OSISAF-SIT in the SSMIS period (2006-2009) and IFREMER-A (2012-2015) show the lowest MYI extent values. Otherwise, the MYI extent from the different SIT products generally correspond to the NSIDC-SIA extents of sea ice of more than 2-3 years.

Daily MYI extent variations of KNMI-Q and -O, IFREMER-Q and Zhang-SIT agree well with that of NSIDC-SIA. C3S- and OSISAF-SIT show larger discrepancies and temporal variabilities than other products, especially C3S-1. Combining with the information in Fig. 1, we can find that KNMI- and IFREMER- and Zhang-SIT based on C-band scatterometer show larger discrepancies than using Ku-band scatterometer, especially in early winter months, and that OSISAF-SIT shows smaller discrepancies since using backscatter data (2010). Among all, the largest difference in daily MYI extent reaches 4.5×10^6 km2. In C3S-1, -2 and OSISAF-SIT, the average extent from the Amb class is 0.21, 0.26 and 0.28×10^6 km2, respectively. The MYI extent temporal patterns of KNMI-Q and -O (Ku-band) are roughly consistent with IFREMER-Q (1999-2008) and Zhang-SIT, with differences varying between 0.01×10^6 km2 and 0.6×10^6 km2.

3.1.2 Monthly MYI extent variation

Monthly average MYI extent of all the SIT and SIA products is presented in Fig. 4, differing by 0.6×10^3-3.6×10^6 km^2. The comparison is demonstrated in three months—November, January and April, on behalf of early, mid- and late winter, respectively. Overall speaking, the spread of MYI extent from all the SIT products is the smallest in January. This is expected from the cold temperatures and stable physical properties of sea ice in mid-winter, which leads to small uncertainties of ice type discrimination. Among the three stages of winter, spread of the various SIT products is the largest in early winter, while the ambiguous extent in C3S- and OSISAF-SIT (shaded area in Fig. 4) is the largest in late winter. Both indicate the difficulties and large discrepancies of SIT products in transition between summer and winter.

For the inter-annual evolution of MYI extent, KNMI-Q, -O, IFREMER-Q, -A and Zhang-SIT agree well with NSIDC-SIA, with modest discrepancies in all stages of winter. Although the evolution of MYI extent from KNMI-A shows the largest discrepancy in early winter, it demonstrates high consistency with NSIDC-SIA in mid- and late winter. Overall speaking, C3S- and OSISAF-SIT show most distinct variations, with remarkably different inter-annual pattern in 2006-2008, in late winters of 2016-2018, and for C3S-SITs in 2001-2003 and early winter in 2004.

3.2 Spatial analysis

3.2.1 Regional MYI extent evolution

To further explain the classification discrepancies between products, we divided the Arctic into three regions (Fig. 2) and analyzed the regional evolution pattern (Fig. 5). Overall, the MYI extent in CAO and ESS shows consistently decreasing trend,

https://doi.org/10.5194/tc-2022-95
Preprint. Discussion started: 19 May 2022

while that in BS keeps constant or increasing. The former is mainly resulted from the outflow of MYI to more southern regions, following the Transpolar Drift Stream, while the latter is predominately attributed to the highly dynamic ice regime in the area, driven by the Beaufort Gyre.

In the winters of 1999-2018, most SIT products show similar trends in CAO region, while exhibiting varying evolution trends for early and late winter in BS and ESS regions. For instance, the anomalously large MYI extent from KNMI-SIT in October and November as mentioned before is mainly resulted from the BS and ESS regions. The large underestimations of MYI extent for OSISAF-SIT in CAO and BS before 2010 is for the early period of the product before inclusion of scatterometer data and algorithm upgrades. C3S-SITs show striking MYI extent fluctuations in 2001-2004 in BS and ESS which show that the distinct inter-annual pattern seen in Fig. 4 is mainly originating from these regions. For both C3S- and OSISAF-SITs, the late-winter increasing trend in 2016-2017 (Fig. 3) is seen for all three regions, however mostly pronounced in BS and ESS regions.

3.2.2 SIT distribution maps

The classification results of SIT products are directly mapped on the perspective of the Arctic to make the inter-comparison of SIT spatial distribution more intuitive. Fig. 6 and 7 show the available SIT and SIA distribution maps in the winters of 2001 and 2007, 2011 and 2016, respectively. Maps of these dates are selected to present typical discrepancies of SIT products as mentioned in previous sections (see Fig. 3 and 5).

In Fig. 6 a-e, the SIT distribution maps of five products on October 17, 2001 are shown for visual analysis. C3S-SITs show obviously less MYI than KNMI-Q, IFREMER-Q and NSIDC-SIA, while the latter three exhibit a quite consistent SIT distribution pattern. The discrepancy of MYI extent between C3S-SITs and NSIDC-SIA is up to $3.31\times 10^6 km^2$. In Fig. 6 a and b (along with Fig. A1 a-d, f-i in Appendix), the discontinuous FYI delineation in the inner part of MYI pack is well demonstrated, which explains the daily MYI extent fluctuation in C3S-SIT. On the other hand, IFREMER-Q shows constantly less MYI than KNMI-Q in the transition zone of MYI and FYI in BS, in good agreement with their difference as shown in Fig. 5.

Fig. 6 f-m show the classification maps of C3S-1, -2, OSISAF-SIT, IFREMER-Q, KNMI-Q, -A, Zhang-SIT and NSIDC-SIA on November 13, 2007. As presented in last section, the MYI extent of KNMI-A is much larger than other products in early winter, with MYI widely distributed in the peripheral seas of the Arctic basin (Fig. 6 j). In comparison, KNMI-Q has the second largest MYI coverage among the seven SIT products, with exceptional MYI distributed in the Arctic peripheral seas such as ESS. Other five SIT products show generally consistent SIT distribution with NSIDC-SIA. Minor differences are found in BS. Additionally, C3S- and OSISAF-SIT show notably less MYI in the Fram Strait.

The classification maps in Fig. 7 a-h demonstrate a typical scenario with small MYI extent. In the maps of March 31, 2012, the SIT distribution from SIT products is not so consistent with that from NSIDC-SIA except C3S-SIT. The consistent SIT distribution between NSIDC-SIA and C3S-SIT is also reflected in the MYI extent. The MYI extent for NSIDC-SIA is about

https://doi.org/10.5194/tc-2022-95
Preprint. Discussion started: 19 May 2022

1.99× 10^6 km2, whereas the weekly MYI extent is 1.99 to 2.34× 10^6 km2 and 1.70 to 2.07× 10^6 km2 for C3S-1 and -2, respectively. KNMI-O, OSISAF- and Zhang-SIT show very similar distribution pattern, with MYI extent of about 1.5× 10^6 km2 in the Arctic basin. IFREMER-A shows the smallest MYI extent (1.06× 10^6 km2). KNMI-A differs substantially from other SIT products as in other case (e.g., Fig. 6 f-m). However, the difference is mainly from the Barents and Kara Seas in this case, not the central Arctic as in other case. Overall, large discrepancies are found among the SIT types, mainly in the BS region.

Fig. 7 i-m shows the classification of C3S-1, -2, OSISAF-, Zhang-SIT and NSIDC-SIA on Mar. 31, 2017. In this month, C3S- and OSISAF-SIT show consistent SIT distribution with NSIDC-SIA except in BS where the MYI is overestimated compared to NSIDC-SIA. This overestimation of MYI can explain the abnormal increasing trend during winter 2016-2017 of the Arctic MYI extent in C3S-SIT and OSISAF-SIT seen in Fig. 3 and with consideration of the regional increasing MYI extent in BS in the winter 2016-2017 (Fig. 5). Furthermore, the thin tongue-shape MYI distribution extending across ESS and BS is not well preserved in Zhang-SIT.

3.3 Validation based on SAR

In this section, SIT products are evaluated using information interpreted from RS-1 and Sentinel-1 SAR images. Five cases are addressed in this study to present SIT distributions under different conditions. Cases in early and late winter are selected to verify situations with notable discrepancies of SIT products, whereas cases in mid-winter are included to explore exact performances of SIT products under relatively steady circumstance.

The comparisons present enlarged zooms of areas with pure ice types and their backscatter signatures. Characteristics of brightness, texture, geometric shape and context in SAR images are the basis for visual interpretation. The NSIDC-SIA product, air temperature and sea surface wind from reanalysis data, and in some cases ice drift product were used to provide additional information for visual analysis.

3.3.1 Cases in early winter

A typical scene of early winter in MIZ is shown in Fig. 8. Compacted ice edge with relatively high backscatter could be observed across the image. In area D, open water manifests high backscatter because of the high wind speed (over 15m/s). Sea ice in the west part (area C) with coarse texture appears to be MYI. In the upper part of image (represented by area A), the coarse texture and darker backscatter signature than area C makes it more likely to be MYI, which drifts from the central Arctic. At the margin of sea ice and the northeast corner (area B), the texture is quite smooth, which could be interpreted as newly generated FYI.

The SIT distribution from Zhang-SIT basically agrees with the SAR image in this case, though it partly misclassifies FYI as open water or MYI (e.g. area B and the MYI block between areas A and B). IFREMER-Q fails to discriminate the boarder between sea ice and ocean. Compared with the SAR image, MYI distribution of IFREMER-Q shows relatively underestimation

https://doi.org/10.5194/tc-2022-95
Preprint. Discussion started: 19 May 2022

in area A. C3S-1, -2 and OSISAF-SIT also underestimate MYI in area A and C (note that scatterometer data is not used in OSISAF-SIT in 2007), identifying slightly less MYI compared to IFREMER-SIT. On this day, the wind field was dominated by strong (~15 m/s) southerly wind which may explain some of the disagreements seen in daily averaged products in regions close to a border between classes. KNMI-SITs overestimate MYI generally. The overestimation is more extensive when using ASCAT (C-band) data (KNMI-A). NSIDC-SIA also overestimates MYI, which might be caused by the oldest ice age assignment of grids and the weekly resolution of the product.

Fig. 9 illustrates a case in the East Siberian Sea in November. The air temperature was below −10℃. The wind speed and ice drift speed in the west part were relatively higher than that in the east part. A bright longitudinal feature is clearly shown in the SAR image. It could be identified as MYI with the bright backscatter and coarse texture (area A). In area D, rounded MYI floes can be identified. The east and west part shows low backscatter and smooth texture (enlarged in areas B and C, respectively), which are typical feature of FYI. Backscatter signature in area B is brighter than that in C, influenced by incidence angle.

SIT distribution patterns of C3S-SITs agree best with the SAR image. Slightly underestimation of MYI can be found in OSISAF-SIT in areas A and D (scatterometer data is used in this case). KNMI-A largely overestimates MYI, especially in the west part of SAR image. Zhang-SIT totally ignores the MYI pack (thin MYI tongue across ESS, similar as the case in Fig. 7 i-m), and this error lasts for the whole winter. The MYI underestimation in NSIDC-SIA can partly be resulted from its weekly temporal resolution.

3.3.2 Case in late winter

A Sentinel-1 image of a scene in southern part of ESS and near the coast, acquired on April 27, 2015, is shown in Fig. 10. The air temperature was around −10℃. The wind speed and sea ice drift speed were relatively low. The elongated bright feature across the central part of SAR image appears to be MYI, with clear floe structure observed in area B. Coarse texture and bright backscatter signature can be found south of the island in the SAR image (area C), indicating MYI in this area. Area A could be deformed FYI considering the smooth net-like texture and bright linear feature. Area D appears be FYI considering the smooth texture and overall dark backscatter signature.

The MYI distribution pattern of KNMI-A resembles the SAR image, with slight overestimation of MYI in the northern part of the image and underestimation of MYI east of the island. IFREMER-A and Zhang-SIT both completely ignore the MYI pack, and this error lasts for the whole winter. C3S-1, -2 and OSISAF-SIT manage to identify MYI southeast of the island and FYI in area A, and to some extent captures the elongated thin MYI feature northeast of the image (partly classified as Amb. However, they underestimate MYI in area B and overestimate MYI in the southern part (area D). NSIDC-SIA slightly underestimates MYI in this case.

https://doi.org/10.5194/tc-2022-95
Preprint. Discussion started: 19 May 2022

3.3.3 Cases in mid-winter

Cases in mid-winter focus on the transit zones between MYI and FYI, for better comparison of steady discrepancies among SIT products.

315 Fig. 11 shows the validation and comparison of five SIT products, with SAR image located in the region across BS and ESS and obtained on February 14, 2007. A large area of MYI with high backscatter, ice floe structure and coarse texture could be observed in the center of the SAR image (Area B). Areas A and C present low backscatter and smooth texture, which are typical characteristics of FYI. The backscatter in Area D is slightly higher, however its smooth texture makes it more likely to be FYI.

320 The general SIT distribution patterns of KNMI-Q and Zhang-SIT are basically consistent with the SAR image. IFREMER-Q, C3S-1, -2 and OSISAF-SIT (radiometer-only period) ignore the MYI pack in this area, and this regional scale misclassification of MYI holds through the whole winter. Compared to the SAR image, the MYI pack in NSIDC-SIA is overestimated in the northern part of the image (area A), which can be caused by the different temporal resolution.

The last case acquired on February 16, 2008 is shown in Fig. 12. The MYI feature is clear in the northeast part of SAR image,
325 so as the FYI in the southwest part. Areas A and D feature round MYI floe, and area C presents typical characteristics of FYI, smooth texture and low backscatter. Area B shows a mixture of FYI and MYI, with MYI in the southeast part and FYI for the rest.

In this case, all the SIT products agree generally well with the SAR image except OSISAF-SIT, which fails to identify the MYI floes in the northeast part. Due to the finer resolution, more detailed SIT distribution is preserved in Zhang-SIT. Slight
330 underestimation of MYI can be found in IFREMER-Q (area A). KNMI-A identifies FYI in area B better than KNMI-Q, otherwise the two KNMI SIT products are very similar. C3S-SITs are generally consistent with the SAR image however have slight misclassifications of the ice floe structure which may be due to the coarse spatial resolution of these products. C3S-1 misidentifies FYI as MYI in area C, whereas C3S-2 misclassifies MYI as FYI in area A. Despite a westward shift, the SIT distribution pattern from NSIDC-SIA is overall similar as the SAR image and indicate a generally older type of MYI (> 3
335 years).

Performances of SIT and SIA products in the above five cases are summarized in Table 2. In all the cases, NSIDC-SIA can generally capture the SIT distribution pattern meanwhile exhibits slight over- or underestimation of MYI because of the ice age assignment of the oldest ice and weekly temporal resolution. These results agree with previous studies (Korosov, Rampal, et al. 2018, Ye, Shokr, et al. 2019) and once again confirm the usage of SIA product as a cross-validation dataset.

340 In the two cases of early winter (Case 1 and 2, Fig. 8 and 9), C3S-SITs have overall the best performances with a slight underestimation of MYI in Case 1 due to a northward shift of the MYI edge which can be explained by the persistent strong southerly wind. In Case 3 and 5, C3S-SITs to some extent capture the SIT distribution but do not come out best under different

https://doi.org/10.5194/tc-2022-95
Preprint. Discussion started: 19 May 2022

circumstances. Between the two products of C3S-SITs, C3S-2 performs slightly better than C3S-1 with more alike SIT distributions with the SAR image in cases 3 and 5 (Fig. 10 and 12). However, the improvement is in these five cases insignificant.

As the only near-real-time operational product, OSISAF-SIT tends to underestimate MYI in most of the cases especially for the early period before inclusion of scatterometer data and dynamically updated PDFs (Case 1, 4 and 5). OSISAF-SIT shows better performance with more recent upgrades of the algorithm. This can also be found in the MYI extent time series (Fig. 3 and 4), where the MYI extent from OSISAF-SIT is smaller than that from most of the SIT products but less so after 2010.

KNMI-SITs show consistent or overestimated MYI distribution in the five cases. Such overestimation of KNMI-SITs, especially KNMI-A, can be found in almost all the winter months. This is well reflected in the extraordinary large MYI extent of KNMI-A in November (Fig. 4, upper panel), which is attributed to the misclassified MYI in the peripheral seas of the Arctic Basin (Fig. 5).

IFREMER-SITs tend to underestimate MYI in several cases as seen in both the time series of MYI extent and in the case studies. In cases 1 and 5 (Fig. 8 and 12), the MYI distribution from IFREMER-Q SIT agrees generally well with the SAR images, with only slight underestimation of MYI. However, open water is misclassified as FYI even in case 1, which is not found in any other SIT products and cases.

Zhang-SIT performs well in the QSCAT period (cases 1, 4 and 5) with a slight underestimation of the marginal ice zone in Case 1. It however fails to identify the MYI within the FYI pack in the ASCAT period (cases 2 and 3). Such pattern can also be reflected in the monthly MYI extent time series (Fig. 4), where the difference between Zhang-SIT and NSIDC-SIA is minimal before 2009 and increases after 2009.

4 Discussion

Performances of SIT products could be attributed to the following factors: 1) input parameters, 2) classification methods, and 3) correction schemes in post-processing procedure. For further discussion, we analyzed the five serial SIT products from the above three perspectives (Table 3).

4.1 Input parameters

The efficacy of input parameters is dependent on the capability to separate and stability of the sea ice types in question. For instance, the contrast between MYI and FYI is high in the GR_{37v19v} (and GR_{19v37v}) fields. This parameter can be impacted by atmospheric factors (e.g. cloud liquid water) although the impact is less for this gradient spectral ratio than for absolute brightness temperatures from passive microwave horizontal polarized or high frequency channels, Also, this parameter can be impacted by surface features (e.g. snow properties, ice layering effects) during the winter season (Comiso 1983, Rostosky, Spreen, et al. 2018, Ye, Shokr, et al. 2019). In the beginning and ending stage of winter, the variability of GR_{37v19v} can be

https://doi.org/10.5194/tc-2022-95
Preprint. Discussion started: 19 May 2022

significant when air temperature fluctuates around freezing point and triggers snow metamorphism. This can partly explain the extensive MYI underestimation in the CAO region from C3S-SIT in October (Fig. 5 and 6), and the MYI overestimation in BS and ESS in the second half winter (Fig. 7). Such misclassification in C3S-1 is mitigated in C3S-2 due to the temperature correction scheme and the upgraded tuning of atmospheric correction for Tb with the ERA5 reanalysis data. Another example is the backscatter (σ^0), which has good separability between MYI and FYI. Backscatter is impacted by surface roughness. As a result, deformed FYI, the backscatter of which is relatively high, can be misclassified as MYI when using backscatter. In comparison, the separability is better at Ku-band than C-band. Products using backscatter of Ku-band generally performs better than those of C-band, e.g. KNMI-, IFREMER-, and Zhang-SIT. However, C-band backscatter could identify FYI more accurately under certain circumstances, e.g. small FYI floes in MYI pack (Case 5, Fig. 12).

It has been confirmed that combination of radiometer and scatterometer data helps to identify ice types due to their complementary information (Yu, Clausi, et al. 2009, Aaboe, Sørensen, et al. 2021). This statement holds under most conditions in this study (Zhang-SIT in Case 4 and 5, Fig. 11 and 12). However, when both passive and active microwave signatures behave anomalously, such combination does not help to mitigate the misclassification problems without regulating rules of priority between the two as is included in the most recent OSISAF-SIT version (since 2020) (Girard-Ardhuin and Ezraty 2012). In peripheral sea that is ice-free during summer, introducing backscatter does not help to improve ice type identification in OSISAF-SIT and Zhang-SIT (Case 2, Fig. 9). In Beaufort and East Siberian seas in late winter, employing Tb measurements even lead to worse classification, and the SIT identification advantage of scatterometer data is lost in the blend (Case 3, Fig. 10). It indicates that simple data combination does not necessarily imply better classification results.

4.2 Classification methods

The representativeness of training datasets and the efficiency of classification methods are crucial for ice type classification. Most SIT products are based on a priori "training" datasets. Some use fixed threshold classification algorithm, while others employ dynamic threshold to account for the variability of training dataset, seasonality and shift in sensor types. For the former, the algorithm works relatively well under conditions similar as the training dataset, however it gives anomalous SIT distribution results in other conditions. For instance, KNMI-SIT uses fixed threshold extracted from mid-winter. Extensive anomalous SIT misclassification is found in the beginning winter, when backscatter characteristics of MYI and FYI vary significantly in different stages of winter, especially based on ASCAT. For the latter, the approach takes sea ice variabilities into account, however it introduces temporal instability. IFREMER-SIT uses a set of thresholds varying with time and the MYI extent sometimes shows high-frequency oscillations (e.g., in 2008 April, see Fig. 3 and A2). C3S- and OSISAF-SIT derive PDF of FYI and MYI from daily training data of fixed target areas. The daily PDFs of the parameter GR_{37v19v} for MYI are highly variable [55]. We speculate this is because the sample area of MYI is susceptible to the change of surface features such as snow properties. Microwave characteristics of the ice samples from a fixed region may not be representative of the

https://doi.org/10.5194/tc-2022-95
Preprint. Discussion started: 19 May 2022

whole Arctic Basin, leading to occasionally extensive misclassifications (see Case 3, 4 and 5, Fig. 10, 11 and 12). This leads to SIT distribution with high-frequency oscillations and large inter-annual variabilities in the C3S and OSISAF-SIT.

Adaptive clustering algorithm is used in Zhang-SIT, without prior training data. The classification depends on the clustering pattern of the two-dimensional scatter of Tb and backscatter. Compared to the QSCAT period (2002-2009), Zhang-SIT shows more anomalous fluctuations and fails to identify thin MYI tongue in peripheral seas in the ASCAT period (2009-2020). This can be partly explained by the large loss of sea ice in summer of 2007, which changes the backscatter distribution mode of Arctic sea ice and makes the separation between FYI and MYI more obscure, especially from ASCAT data (Belmonte Rivas, Otosaka, et al. 2018, Zhang, Yu, et al. 2019).

4.3 Correction schemes

Post-processing correction plays an important role in SIT products. For more accurate SIT distribution, various correction schemes are implemented in the SIT products. These correction schemes can be summarized as follows: 1) corrections based on geographic mask, 2) correction based on statistical threshold, 3) corrections based on temperature records and the temporal variabilities of SIT distribution, 4) corrections based on fixed tolerance of ice motion and preceding results, and 5) corrections based on spatial filtering.

The first kind of correction scheme, a mask of the Arctic basin, has been used in C3S, OSISAF- and KNMI-SIT to remove unphysical MYI signature in Greenland, Kara, Barents and Chukchi Seas. This is restricted to these areas therefore could not modify classification results within the central Arctic. Statistical thresholds in C3S- and OSISAF-SIT exclude extreme values that are likely to cause misclassification, e.g. values in the long-tail of MYI PDF giving rise to erroneously classified ice along the ice edge. These two kinds of corrections exclude misclassification cases in specific regions and thus have smaller impact on the overall SIT distributions.

The temperature-based correction in C3S-2 aims to reassign erroneously classified FYI impacted by transient warm air intrusions. Therefrom the discontinuous FYI delineation in the inner part of MYI pack is partly mitigated compared to C3S-1 (Fig. A1). In Zhang-SIT, an ice motion confining procedure is introduced to eliminate anomalous MYI overestimation. However, wrong identification or reassignment from MYI to the category of FYI might lead to continuous underestimation. Another correction used in Zhang-SIT is the median filter correction, which is employed to remove large unusual spatial variations. The two correction schemes in Zhang-SIT help to mitigate the afore-mentioned problem. However, inappropriate thresholds in them may lead to over-correction problem, making Zhang-SIT incapable to identify thin MYI tongue in peripheral seas during winter season (Case 2 and 3, Fig. 9 and 10).

Apart from the above three factors, the five series SIT products differ in other ways they are defined. The seasonal length of classification differs from the “all year” KNMI products to a limited winter period for the other products (see Table 1). Typically, in early and late winter larger uncertainties are seen due to surface melting over sea ice and atmospheric influence.

https://doi.org/10.5194/tc-2022-95
Preprint. Discussion started: 19 May 2022

435 Some SIT products do not provide data in these months (e.g. Zhang-SIT in October), and an inter-comparison of the performance in such conditions cannot be fully evaluated.

In addition, the SIT products differ in the time periods they cover and their spatial resolutions. For instance, the main purpose of the C3S-SITs is to get the longest possible climate data record (more than four decades and updated to present time) wherefore only passive microwave radiometers are implemented. The disadvantage of this is the resulting coarse spatial 440 resolution. The spatial resolution impacts the inter-comparison and thus should also be considered. In this study, the spatial grid resolution of the SIT products ranges between 4.45 km and 25 km, however their true spatial resolution (foot print) is often even larger, e.g. as high as ~40 km for the SSM/S and SSMIS based products (C3S-SITs and early OSISAF-SIT). These different resolutions are reflected in the SIT distribution and how well the products capture smaller scale features, like ice floes, ice edges between classes, etc. For instance, more detailed information can be found in Zhang-SIT in case 5 (Fig. 12), whereas 445 the C3S- and OSISAF-SITs did not resolve this ice floe pattern just as well. However, finer resolution related to high frequency channels does not necessarily mean high accuracy since more noise may be introduced with higher frequencies.

5 Conclusion

Arctic sea ice cover has decreased dramatically over the past few decades, especially MYI. The change of SIT distribution 450 impacts the Arctic and global climate. However, systematical inter-comparison and analysis for SIT products are still lacking. In this paper, nine SIT products based on five retrieval approaches were inter-compared through temporal and spatial analysis. Performances of them are evaluated qualitatively using SAR images. Differences among the SIT products in daily MYI extent within Arctic Basin can reach 4.5×10^6 km^2, while that in monthly data varies between 0.6×10^3 km^2 and 3.6×10^6 km^2. Large discrepancies occur in October, November and April, mainly in the Beaufort Sea and East Siberia Sea. Overall, 455 performances of the SIT products can be summarized as follows:

1) C3S-SIT has the longest and most complete temporal record however large temporal variability and anomalous (flat or increasing) trends within certain years. The fluctuation and misclassification are likely attributed to the single classification parameter from dynamic training datasets, which are vulnerable to environment changes and may not be representative for the entire Arctic. C3S-2 performs slightly better than C3S-1 with less misclassification and smaller 460 temporal variability, which most likely is resulted from the upgrades of auxiliary data in atmospheric correction and temperature-based correction;
2) OSISAF-SIT is a near-real-time product and the archive data has discontinuities due to regular upgrades. It shows overall underestimation of MYI during radiometer-only period (pre-2010). At present, OSISAF-SIT uses additional scatterometer data and finer spatial resolution radiometer data. The recent version performs better but still presents 465 fluctuations and in some cases instable classification;
3) For pure scatterometer-based products, KNMI-SIT tends to overestimate MYI while IFREMER-SIT underestimates MYI overall. Thresholds used in the classification algorithms play an important role in these two SIT products. KNMI-

https://doi.org/10.5194/tc-2022-95
Preprint. Discussion started: 19 May 2022

SIT performs well in deep winter. However, MYI extent is overestimated in the Arctic peripheral seas in October and November, especially the products with C-band scatterometer input (e.g. KNMI-A);

4) Zhang-SIT exhibits distinct performances in the two scatterometer periods, with good performance in 2002-2009 (Ku-band scatterometer) while underestimation of MYI and more anomalous fluctuations after 2009 (C-band scatterometer). During the latter period, it shows difficulties in detecting thin tongue-shape distribution of MYI in the Arctic peripheral seas, partly influenced by the excessive correction during post-processing.

Among all the SIT products, KNMI-Q, -O and Zhang-SIT (especially during QSCAT period) perform the best. This confirms that QSCAT is very capable in distinguishing the ice types. KNMI-A generally present overestimation of MYI and occasionally have extensive misclassification, while IFREMER-SITs show overall underestimation. C3S- and OSISAF-SIT have large daily variability and occasionally present extensive misclassification with higher uncertainties. Based on the above inter-comparisons, we further investigate the factors that may impact the SIT production. The main findings can be summarized as follows:

- Ku-band scatterometer generally performs better than C-band scatterometer on ice types discrimination. However, the latter sometimes could identify FYI more accurately, e.g. small FYI in MYI pack;
- Simple combination of scatterometer and radiometer data is not always beneficial without further rules of priority between the two. In peripheral seas in early winter, introducing backscatter does not help for better ice type identification. In Beaufort and East Siberian seas in late winter, performance of the SIT products using combined data is weighed down by the radiometer data, the MYI identification advantage of backscatter diminishes;
- The representativeness of training data and the efficiency of classification method are crucial for ice type classification. Fixed thresholds extracted from deep winter may not be suitable for the entire winter, while dynamic training datasets could be susceptible to local environmental conditions and introduce temporal instability. On the other hand, adaptive classification method that depends on the clustering pattern of the radiometer and backscatter scatter may be inefficient when the separation between MYI and FYI becomes obscure;
- Post-processing corrections play important roles in SIT products and should be accounted with caution. Excessive post-processing such as ice motion confining could lead to accumulative errors. These post-processing should be flagged in a related product variable.

Accurate estimation of Arctic SIT distribution is crucial for better understanding regional and global climate change, as well as defining sea ice and snow properties for ice thickness retrievals, sea ice models and so on. This study gives a systematic evaluation of the most popular SIT products and provides hints for further improvement of SIT retrieval approach. With the new twin-frequency scatterometer (WindRAD) onboard Fengyun (FY)-3E satellite, the potential of scatterometer on ice type discrimination can be further investigated. On the other hand, the Copernicus Imaging Microwave Radiometer with higher spatial resolution at low frequency channels in near future opens the opportunity of using low frequency microwave measurements for SIT classification (Kilic, Prigent, et al. 2018).

Appendix A

See Fig. A1 and Fig. A2.

https://doi.org/10.5194/tc-2022-95
Preprint. Discussion started: 19 May 2022

Author contribution

Y.Y. designed the experiments and lead the manuscript writing. Y.L. and Y.S. conducted the data analysis. M.S. provided access to the SAR images and contributed to interpretation of the SAR images. Y.L., S.A. and F.G. contributed to result analysis. F.H., X.C. and Z.C. contributed to the research design and results analysis. All co-authors participated in the fruitful discussions and manuscript revision.

Competing interests

The authors declare that they have no conflict of interest.

Acknowledgement

This work is supported by the National Natural Science Foundation of China (Grant No. 42106225), the Innovation Group Project of Southern Marine Science and Engineering Guangdong Laboratory (Zhuhai) (Grant No. 311021008), the National Key Research and Development Program of China (Grant No. 2019YFC1509104) and the Natural Science Foundation of Guangdong Province, China (Grant No. 2022A1515011545). We greatly thank C3S (https://doi.org/10.24381/cds.29c46d83, accessed on 1 April 2022), OSI SAF (https://osi-saf.eumetsat.int/products/osi-403-d， accessed on 1 April 2022), KNMI (https://dataplatform.knmi.nl/dataset/, accessed on 1 April 2022), Fanny Girard-Ardhuin and Zhilun Zhang for providing SIT products. We also thank NSIDC for providing SIA product (https://nsidc.org/data/NSIDC-0611/versions/4, accessed on 1 April 2022), ECWMF for providing ERA5 reanalysis (https://www.ecmwf.int/en/forecasts/datasets/reanalysis-datasets/era5, accessed on 1 April 2022), IFREMER for providing ice drift product (ftp://ftp.ifremer.fr/ifremer/cersat/products/gridded/psi-drift/data/arctic, accessed on 1 April 2022), as well as the ASF and MDA for providing Radarsat-1 and Sentinel-1 images (https://search.asf.alaska.edu/, accessed on 1 April 2022).

References

S. Aaboe, L.-A. Breivik and S. Eastwood (2014). Improvement of OSI SAF Product of Sea Ice Edge and Sea Ice Type. EUMETSAT Meteorological Satellite Conference, Geneva (Switzerland).

S. Aaboe, L.-A. Breivik and S. Eastwood (2016), Global Sea Ice Edge (OSI-402-c) and Type (OSI-403-c) Validation Report, v2.1, EUMETSAT OSI SAF, https://osisaf-hl.met.no/sites/osisaf-hl/files/validation_reports/osisaf_cdop2_ss2_valrep_sea-ice-edge-type_v2p1.pdf,Accessed 1 October 2021.

S. Aaboe, A. Sørensen, T. Lavergne and S. Eastwood (2018), Sea Ice Edge and Sea Ice Type Climate Data Records Algorithm Theoretical Basis Document, v2.2, Copericus Climate Change Service, https://datastore.copernicus-climate.eu/documents/satellite-sea-ice-edge-type/v1.0/C3S_D312a_Lot1.2.2.5-v2_201805_atbd_sea-ice-edge-type.pdf,Accessed 1 October 2021.

https://doi.org/10.5194/tc-2022-95
Preprint. Discussion started: 19 May 2022

S. Aaboe, A. Sørensen, T. Lavergne and S. Eastwood (2021), Sea Ice Edge and Sea Ice Type Climate Data Records Algorithm Theoretical Basis Document, v3.1, Copernicus Climate Change Service, https://datastore.copernicus-climate.eu/documents/satellite-sea-ice-edge-type/v2.0/D1.SIETy.2-v2.0_ATBD-of-v2.0-SeaIceEdgeType-products_v3.1_APPROVED_Ver1.pdf,Accessed 1 October 2021.

M. Belmonte Rivas, I. Otosaka, A. Stoffelen and A. Verhoef: A scatterometer record of sea ice extents and backscatter: 1992–2016, The Cryosphere, 12, 2941-2953,doi: 10.5194/tc-12-2941-2018.

M. Belmonte Rivas, J. Verspeek, A. Verhoef and A. Stoffelen: Bayesian Sea Ice Detection With the Advanced Scatterometer ASCAT, IEEE Transactions on Geoscience and Remote Sensing, 50, 2649-2657,doi: 10.1109/tgrs.2011.2182356.

H. J. Belter, T. Krumpen, L. von Albedyll, T. A. Alekseeva, G. Birnbaum, S. V. Frolov, S. Hendricks, A. Herber, I. Polyakov and I. Raphael: Interannual variability in Transpolar Drift summer sea ice thickness and potential impact of Atlantification, The Cryosphere, 15, 2575-2591,doi: 10.5194/tc-15-2575-2021.

L. N. Boisvert, A. A. Petty and J. C. Stroeve: The impact of the extreme winter 2015/16 Arctic cyclone on the Barents–Kara Seas, Monthly Weather Review, 144, 4279-4287,doi: 10.1175/MWR-D-16-0234.1.

L.-A. Breivik, S. Eastwood and T. Lavergne: Use of C-band scatterometer for sea ice edge identification, IEEE Transactions on Geoscience and Remote Sensing, 50, 2669-2677,doi: 10.1109/TGRS.2012.2188898.

F. Carsey: Summer Arctic sea ice character from satellite microwave data, Journal of Geophysical Research: Oceans, 90, 5015-5034,doi: 10.1029/JC090iC03p05015.

J. Comiso: Sea ice effective microwave emissivities from satellite passive microwave and infrared observations, Journal of Geophysical Research: Oceans, 88, 7686-7704.

J. C. Comiso: Large Decadal Decline of the Arctic Multiyear Ice Cover, Journal of Climate, 25, 1176-1193,doi: 10.1175/jcli-d-11-00113.1.

J. C. Comiso, C. L. Parkinson, R. Gersten and L. Stock: Accelerated decline in the Arctic sea ice cover, Geophysical research letters, 35,doi: 10.1029/2007GL031972.

D. S. Early and D. G. Long: Azimuthal modulation of C-band scatterometer σ/sup 0/ over Southern Ocean sea ice, IEEE Transactions on Geoscience and Remote Sensing, 35, 1201-1209,doi: 10.1109/36.628787.

D. S. Early and D. G. Long: Image reconstruction and enhanced resolution imaging from irregular samples, IEEE Transactions on Geoscience and Remote Sensing, 39, 291-302,doi: 10.1109/36.905237.

C. Emmerson and G. Lahn (2012), Arctic opening: Opportunity and risk in the high north, http://library.arcticportal.org/id/eprint/1671,Accessed 1 October 2021.

R. Ezraty and A. Cavanié: Intercomparison of backscatter maps over Arctic sea ice from NSCAT and the ERS scatterometer, Journal of Geophysical Research: Oceans, 104, 11471-11483,doi: 10.1029/1998jc900086.

C. Fowler, W. J. Emery and J. Maslanik: Satellite-Derived Evolution of Arctic Sea Ice Age: October 1978 to March 2003, IEEE Geoscience and Remote Sensing Letters, 1, 71-74,doi: 10.1109/lgrs.2004.824741.

F. Girard-Ardhuin: Multi-year Arctic sea ice extent estimate from scatterometers onboard satellite since 2000, Journal, C42B-07.

F. Girard-Ardhuin and R. Ezraty: Enhanced Arctic Sea Ice Drift Estimation Merging Radiometer and Scatterometer Data, IEEE Transactions on Geoscience and Remote Sensing, 50, 2639-2648,doi: 10.1109/tgrs.2012.2184124.

S. Hakkinen, A. Proshutinsky and I. Ashik: Sea ice drift in the Arctic since the 1950s, Geophysical research letters, 35,doi: 10.1029/2008gl034791.

M. Hallikainen and D. P. Winebrenner (1992). The physical basis for sea ice remote sensing. Microwave remote sensing of sea ice. F. Carsey. 68: 29-46.

Author, ERA5 hourly data on single levels from 1979 to present., Copernicus Climate Change Service (C3S) Climate Data Store (CDS), 10.24381/cds.adbb2d47,Accessed Date Accessed.

S. Kern, A. Rösel, L. T. Pedersen, N. Ivanova, R. Saldo and R. T. Tonboe: The impact of melt ponds on summertime microwave brightness temperatures and sea-ice concentrations, The Cryosphere, 10, 2217-2239,doi: 10.5194/tc-10-2217-2016.

L. Kilic, C. Prigent, F. Aires, J. Boutin, G. Heygster, R. T. Tonboe, H. Roquet, C. Jimenez and C. Donlon: Expected Performances of the Copernicus Imaging Microwave Radiometer (CIMR) for an All-Weather and High Spatial Resolution Estimation of Ocean and Sea Ice Parameters, Journal of Geophysical Research: Oceans, 123, 7564-7580,doi: 10.1029/2018jc014408.

A. A. Korosov, P. Rampal, L. T. Pedersen, R. Saldo, Y. Ye, G. Heygster, T. Lavergne, S. Aaboe and F. Girard-Ardhuin: A new tracking algorithm for sea ice age distribution estimation, The Cryosphere, 12, 2073-2085,doi: 10.5194/tc-12-2073-2018.

R. Kwok: Annual cycles of multiyear sea ice coverage of the Arctic Ocean: 1999–2003, Journal of Geophysical Research, 109,doi: 10.1029/2003jc002238.

R. Kwok: Arctic sea ice thickness, volume, and multiyear ice coverage: losses and coupled variability (1958–2018), Environmental Research Letters, 13,doi: 10.1088/1748-9326/aae3ec.

R. Kwok and G. F. Cunningham: Variability of Arctic sea ice thickness and volume from CryoSat-2, Philosophical Transactions of the Royal Society A: Mathematical, Physical and Engineering Sciences, 373, 20140157,doi: 10.1098/rsta.2014.0157.

R. Kwok, G. F. Cunningham and S. Yueh: Area balance of the Arctic Ocean perennial ice zone: October 1996 to April 1997, Journal of Geophysical Research: Oceans, 104, 25747-25759,doi: 10.1029/1999jc900234.

R. Kwok, G. Spreen and S. Pang: Arctic sea ice circulation and drift speed: Decadal trends and ocean currents, Journal of Geophysical Research: Oceans, 118, 2408-2425,doi: 10.1002/jgrc.20191.

S.-M. Lee, B.-J. Sohn and S.-J. Kim: Differentiating between first-year and multiyear sea ice in the Arctic using microwave-retrieved ice emissivities, Journal of Geophysical Research: Atmospheres, 122, 5097-5112,doi: 10.1002/2016jd026275.

D. Lindell and D. Long: Multiyear Arctic Ice Classification Using ASCAT and SSMIS, Remote Sensing, 8, 294,doi: 10.3390/rs8040294.

D. B. Lindell and D. G. Long: Multiyear Arctic Sea Ice Classification Using OSCAT and QuikSCAT, IEEE Transactions on Geoscience and Remote Sensing, 54, 167-175,doi: 10.1109/tgrs.2015.2452215.

J. Liu, J. A. Curry, H. Wang, M. Song and R. M. Horton: Impact of declining Arctic sea ice on winter snowfall, Proceedings of the National Academy of Sciences, 109, 4074-4079,doi: 10.1073/pnas.1114910109.

Y. Liu, J. R. Key, X. Wang and M. Tschudi: Multidecadal Arctic sea ice thickness and volume derived from ice age, The Cryosphere, 14, 1325-1345,doi: 10.5194/tc-14-1325-2020.

A. S. Lomax, D. Lubin and R. H. Whritner: The potential for interpreting total and multiyear ice concentrations in SSM/I 85.5 GHz imagery, Remote Sensing of Environment, 54, 13-26,doi: 10.1016/0034-4257(95)00082-C.

D. G. Long, P. J. Hardin and P. T. Whiting: Resolution enhancement of spaceborne scatterometer data, IEEE Transactions on Geoscience and Remote Sensing, 31, 700-715,doi: 10.1109/36.225536.

J. A. Maslanik, C. Fowler, J. Stroeve, S. Drobot, J. Zwally, D. Yi and W. Emery: A younger, thinner Arctic ice cover: Increased potential for rapid, extensive sea-ice loss, Geophysical research letters, 34,doi: 10.1029/2007gl032043.

W. N. Meier, G. K. Hovelsrud, B. E. H. Van Oort, J. R. Key, K. M. Kovacs, C. Michel, C. Haas, M. A. Granskog, S. Gerland, D. K. Perovich, A. Makshtas and J. D. Reist: Arctic sea ice in transformation: A review of recent observed changes and impacts on biology and human activity, Reviews of Geophysics, 52, 185-217,doi: 10.1002/2013rg000431.

I. H. Onarheim, T. Eldevik, L. H. Smedsrud and J. C. Stroeve: Seasonal and Regional Manifestation of Arctic Sea Ice Loss, Journal of Climate, 31, 4917-4932,doi: 10.1175/jcli-d-17-0427.1.

D. Perovich, W. Meier, M. Tschudi, S. Farrell, S. Hendricks, S. Gerland, L. Kaleschke, R. Ricker, X. Tian-Kunze, M. Webster and K. Wood (2019), Sea ice, Arctic Report Card 2019, http://www.arctic.noaa.gov/Report-Card.

A. A. Petty, N. T. Kurtz, R. Kwok, T. Markus and T. A. Neumann: Winter Arctic sea ice thickness from ICESat-2 freeboards, Journal of Geophysical Research: Oceans, 125, e2019JC015764,doi: 10.1029/2019JC015764.

M. B. Rivas, I. Otosaka, A. Stoffelen and A. Verhoef: KNMI-A scatterometer record of sea ice extents and backscatter: 1992–2016, The Cryosphere, 12, 2941-2953,doi: 10.5194/tc-12-2941-2018.

P. Rostosky, G. Spreen, S. L. Farrell, T. Frost, G. Heygster and C. Melsheimer: Snow Depth Retrieval on Arctic Sea Ice From Passive Microwave Radiometers—Improvements and Extensions to Multiyear Ice Using Lower Frequencies, Journal of Geophysical Research: Oceans, 123, 7120-7138,doi: https://doi.org/10.1029/2018JC014028.

J. A. Screen, I. Simmonds, C. Deser and R. Tomas: The atmospheric response to three decades of observed Arctic sea ice loss, Journal of Climate, 26, 1230-1248,doi: 10.1175/JCLI-D-12-00063.1.

M. Shokr, A. Lambe and T. Agnew: A New Algorithm (ECICE) to Estimate Ice Concentration From Remote Sensing Observations: An Application to 85-GHz Passive Microwave Data, IEEE Transactions on Geoscience and Remote Sensing, 46, 4104-4121,doi: 10.1109/tgrs.2008.2000624.

Y. Sun and X.-M. Li: Denoising Sentinel-1 Extra-Wide Mode Cross-Polarization Images Over Sea Ice, IEEE Trans. Geosci. Remote. Sens., 59, 2116-2131,doi: 10.1109/TGRS.2020.3005831.

A. M. Swan and D. G. Long: Multiyear Arctic Sea Ice Classification Using QuikSCAT, IEEE Transactions on Geoscience and Remote Sensing, 50, 3317-3326,doi: 10.1109/tgrs.2012.2184123.

F. J. Wentz: A well-calibrated ocean algorithm for special sensor microwave / imager, Journal of Geophysical Research: Oceans, 102, 8703-8718,doi: 10.1029/96jc01751.

Y. Ye and G. Heygster (2015). Arctic Multiyear Ice Concentration Retrieval from SSM/I Data Using the NASA Team Algorithm with Dynamic Tie Points. Towards an Interdisciplinary Approach in Earth System Science: Advances of a Helmholtz Graduate Research School. G. Lohmann, H. Meggers, V. Unnithan, D. Wolf-Gladrow, J. Notholt and A. Bracher. Cham, Springer International Publishing: 99-108.

Y. Ye, M. Shokr, S. Aaboe, W. Aldenhoff, L. E. B. Eriksson, G. Heygster, C. Melsheimer and F. Girard-Ardhuin: Inter-comparison and evaluation of sea ice type concentration algorithms, The Cryosphere Discuss,doi: 10.5194/tc-2019-200.

P. Yu, D. A. Clausi and S. Howell: Fusing AMSR-E and QuikSCAT Imagery for Improved Sea Ice Recognition, IEEE Transactions on Geoscience and Remote Sensing, 47, 1980-1989,doi: 10.1109/tgrs.2009.2013632.

Z. Zhang, Y. Yu, X. Li, F. Hui, X. Cheng and Z. Chen: Arctic Sea Ice Classification Using Microwave Scatterometer and Radiometer Data During 2002–2017, IEEE Transactions on Geoscience and Remote Sensing, 57, 5319-5328,doi: 10.1109/tgrs.2019.2898872.

Z. Zhang, Y. Yu, M. Shokr, X. Li, Y. Ye, X. Cheng, Z. Chen and F. Hui: Intercomparison of Arctic Sea Ice Backscatter and Ice Type Classification Using Ku-Band and C-Band Scatterometers, IEEE Transactions on Geoscience and Remote Sensing, 1-18,doi: 10.1109/tgrs.2021.3099835.

https://doi.org/10.5194/tc-2022-95
Preprint. Discussion started: 19 May 2022

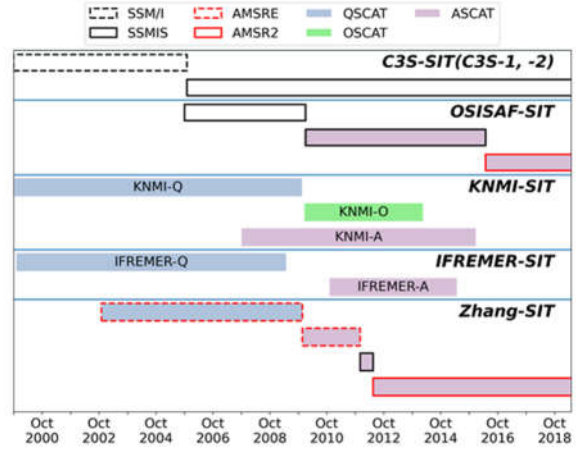

Figure 1: The time lines and satellite data input of nine SIT products used in this study based on five SIT retrieval approaches.

Table 1. Basic information of sea ice type products

SIT products	Covering periods		Satellite inputs	Frequency	Resolution
C3S-SIT	1979-2020	Oct.1-Apr.30	SMMR, SSM/I, SSMIS	daily	25 km
	1978-present	Oct.15-Apr.30	SMMR, SSMI/I, SSMIS	daily	25 km
OSISAF-SIT	2005-present	Oct.1-Apr.30	ASCAT, SSMIS, AMSR-2	daily	10 km
KNMI-SIT	1999-2009	All the year	QSCAT	daily	12.5 km
	2007-2016		ASCAT		
	2010-2013		OSCAT		
IFREMER-SIT	1999-2009	Oct.1-Apr.30	QSCAT	daily	12.5 km
	2010-2015	Nov.1-Apr.30	ASCAT		
Zhang-SIT	2002-2020	Nov.1-Apr.30	QSCAT, ASCAT, ASMR-E, AMSR-2, SSM/I	daily	4.45 km

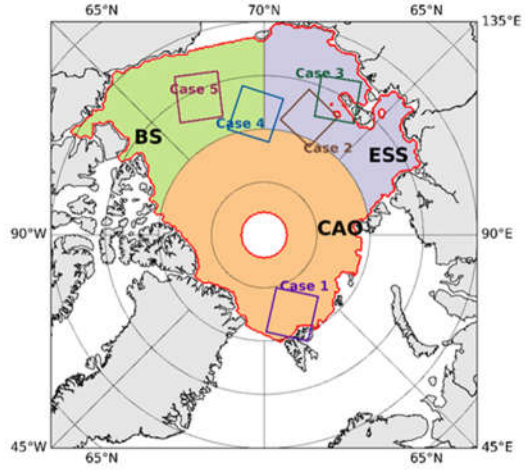

Figure 2: Geographic locations of the SAR images for five cases and outline of the Arctic Basin (red contour, provided by (Belmonte Rivas, Otosaka, et al. 2018)). The Arctic Basin is divided into three subregions: the central Arctic Ocean (CAO), the East Siberian Sea (ESS) and the Barents Sea (BS).

https://doi.org/10.5194/tc-2022-95
Preprint. Discussion started: 19 May 2022

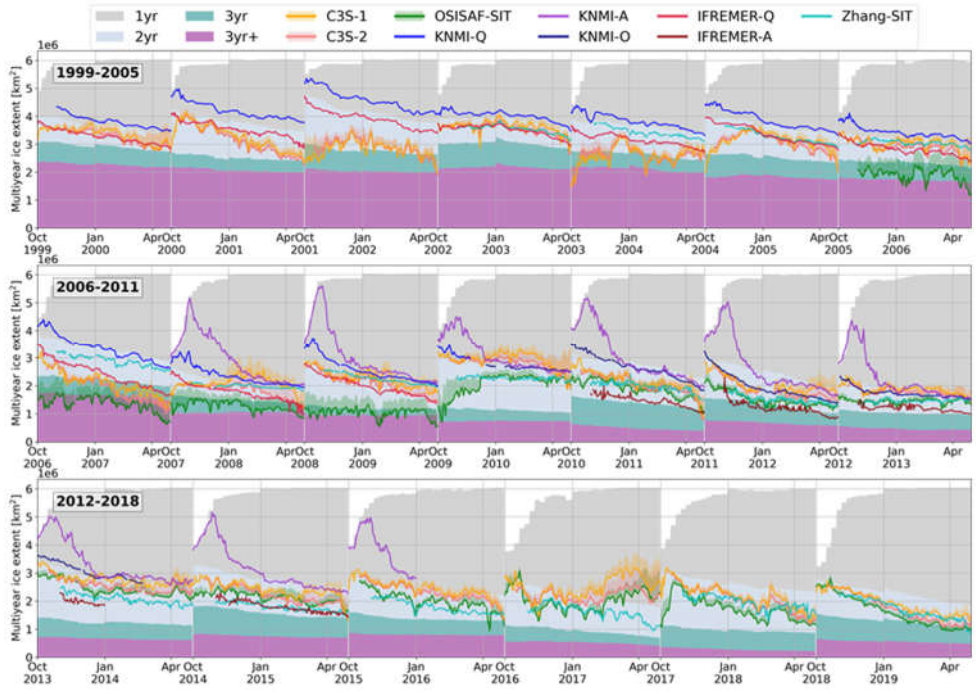

Figure 3: Daily Arctic MYI extent from the SIT and NSIDC-SIA products. Line represents result from SIT product and the shaded area represents the ambiguous extent from Amb class, while the stacked color block represents ice extent with corresponding age from NSIDC-SIA.

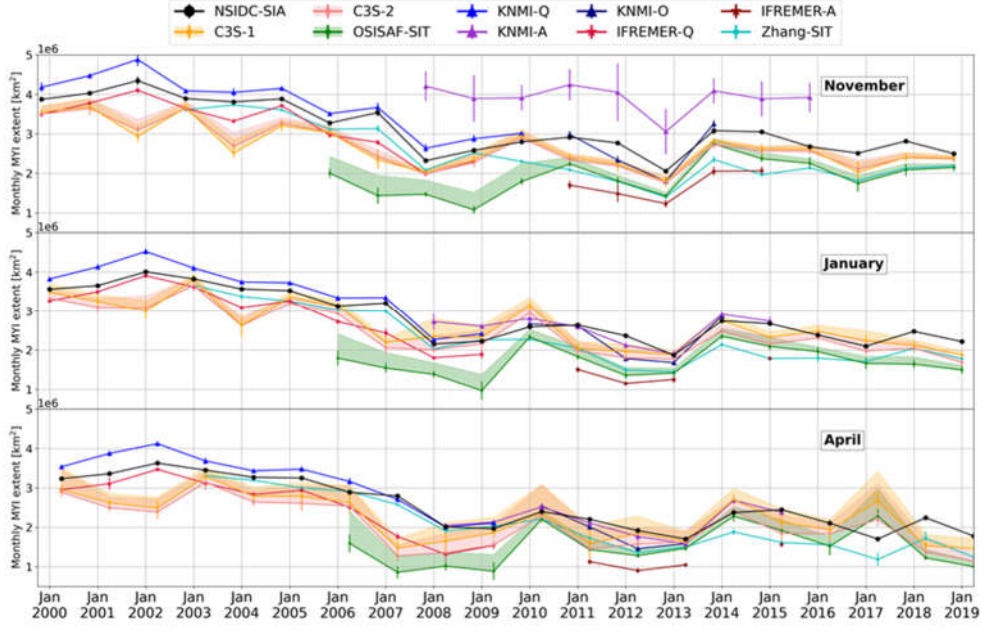

Figure 4: Monthly MYI extent of all the SIT and SIA products in November (top panel), January (middle panel) and April (bottom panel) from November 1999 to April 2019.

https://doi.org/10.5194/tc-2022-95
Preprint. Discussion started: 19 May 2022

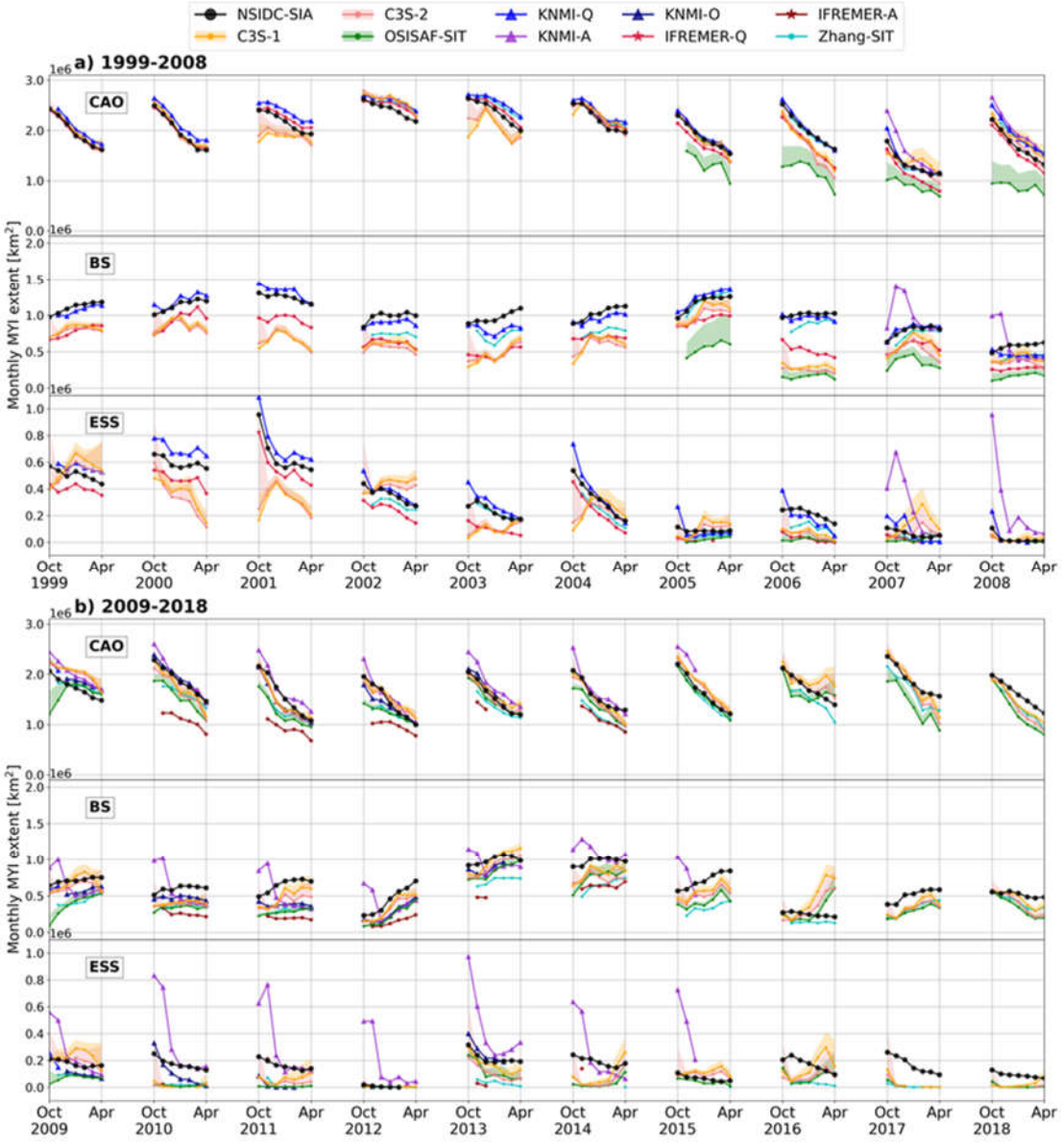

Figure 5: Monthly MYI extent of SIT and SIA products in the central Arctic Ocean (CAO), Beaufort Sea (BS) and East Siberian Sea (ESS) in the years (a) 1999-2008 and (b) 2009-2018.

https://doi.org/10.5194/tc-2022-95
Preprint. Discussion started: 19 May 2022

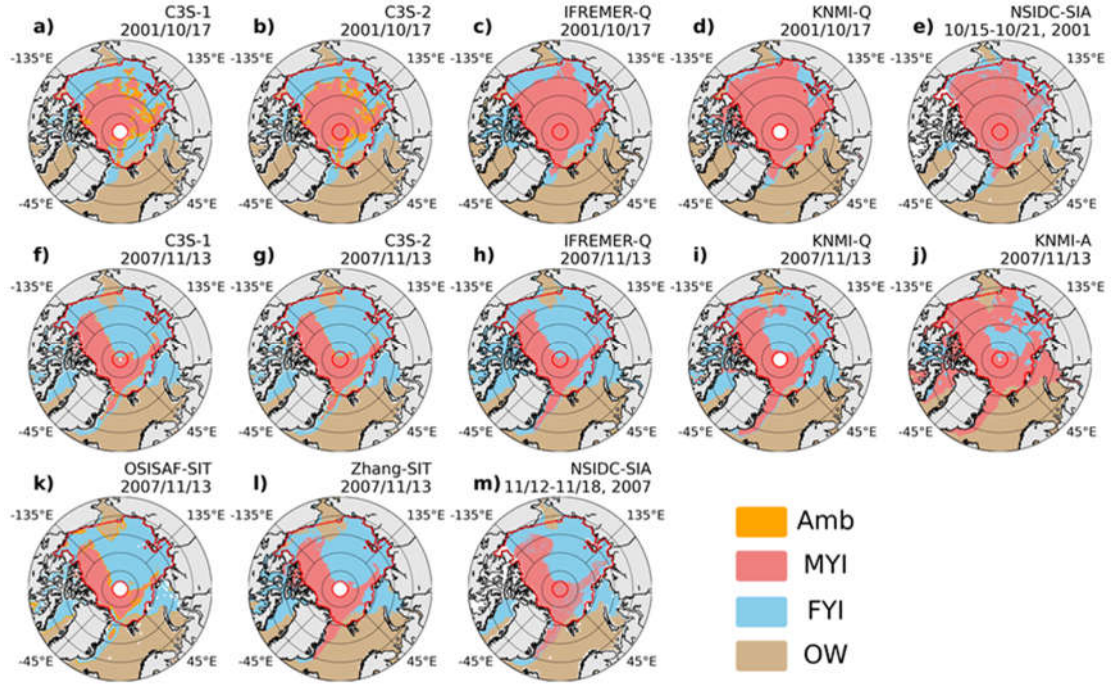

Figure 6: Arctic SIT distribution maps from daily SIT products and weekly NSIDC-SIA product on October 17, 2001 (a-e) and November 13, 2007 (f-m).

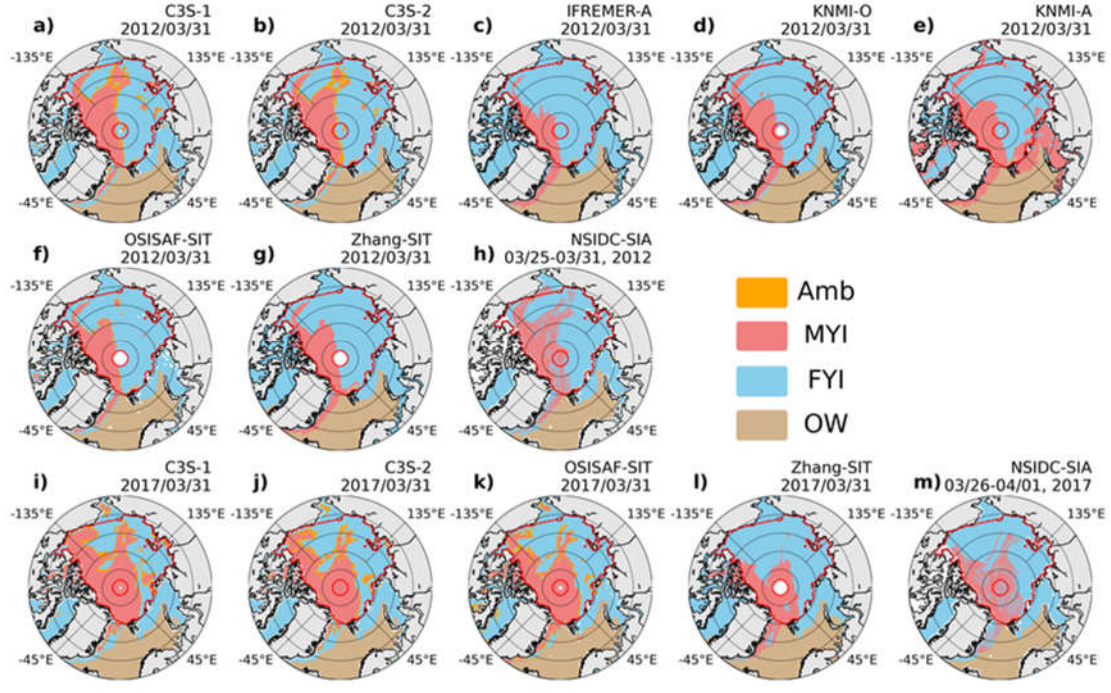

Figure 7: Arctic SIT distribution maps from daily SIT products and weekly NSIDC-SIA on March 30, 2012 (a-h) and March 31, 2017 (i-m).

https://doi.org/10.5194/tc-2022-95
Preprint. Discussion started: 19 May 2022

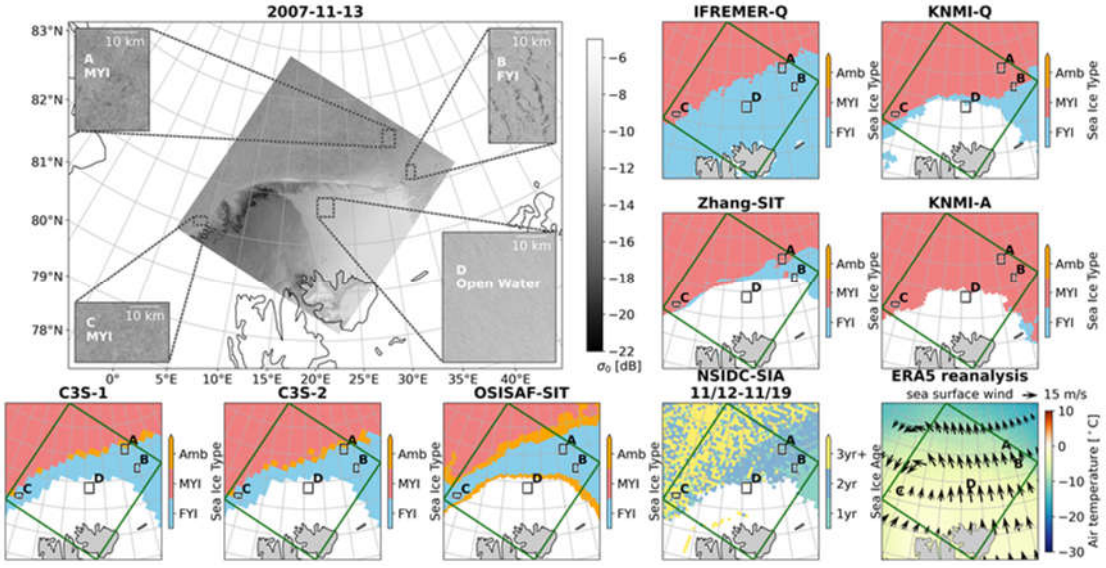

Figure 8: RS-1 image, ice type distribution from seven SIT products (C3S-1, C3S-2, OSISAF-SIT, IFREMER-Q, KNMI-Q, KNMI-A, and Zhang-SIT) and weekly NSIDC-SIA product, along with air temperature and sea surface wind from ECMWF ERA5 reanalysis on November 13, 2007.

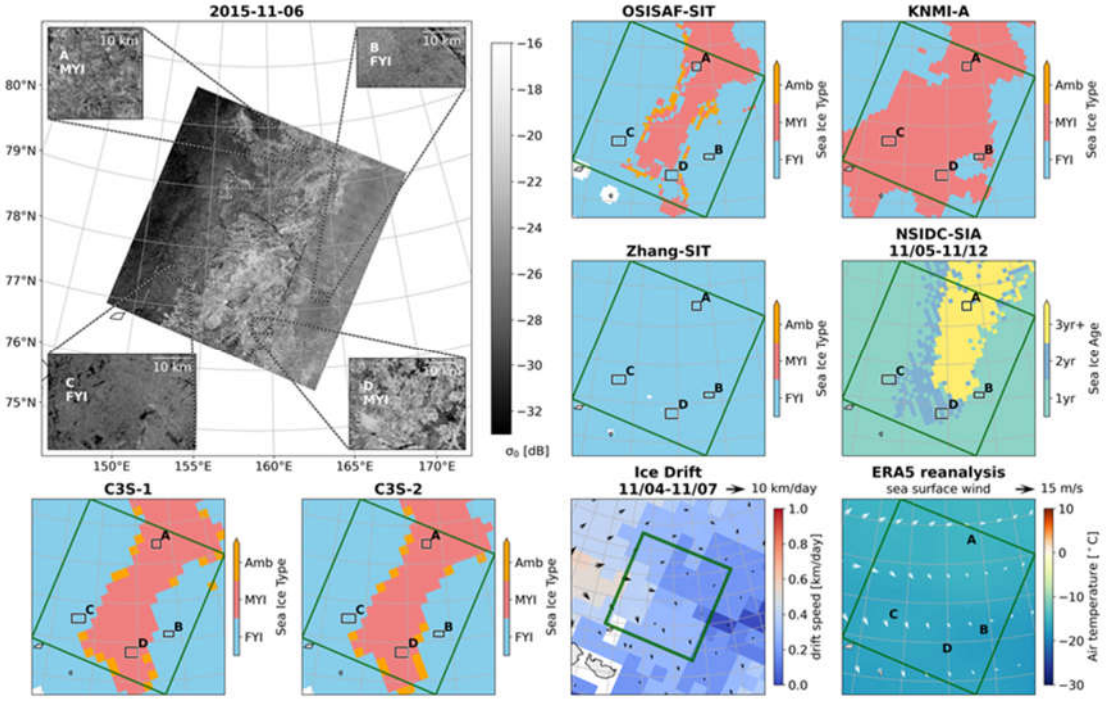

680

Figure 9: HV polarization channel of Sentinel-1 image, SIT distribution from five SIT products (C3S-1, C3S-2, OSISAF-SIT, KNMI-A, and Zhang-SIT) and weekly NSIDC-SIA product, 3-daily ice drift, along with air temperature and sea surface wind from ECMWF ERA5 reanalysis on November 6, 2015.

https://doi.org/10.5194/tc-2022-95
Preprint. Discussion started: 19 May 2022

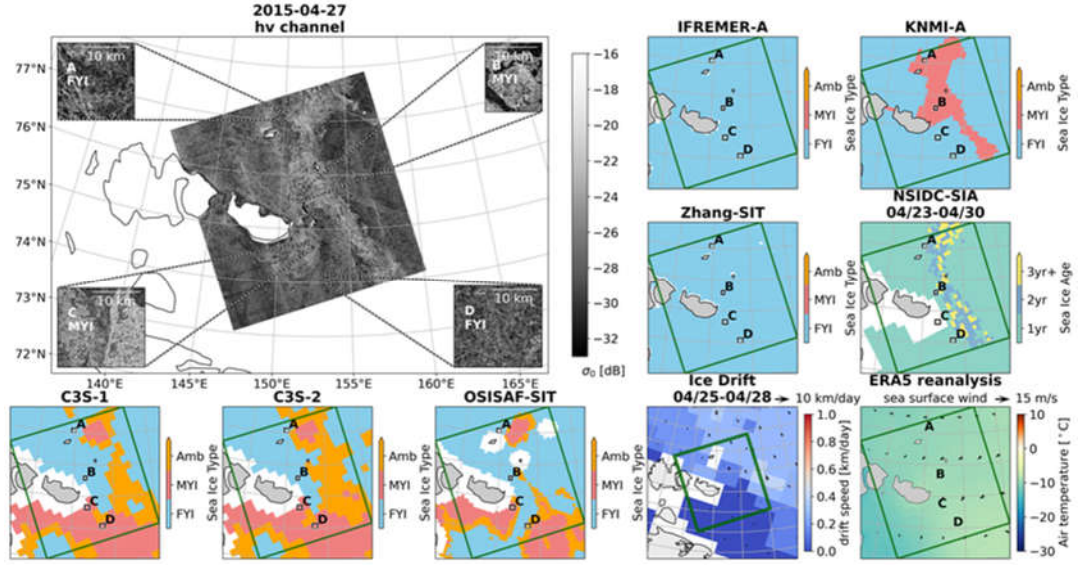

685 **Figure 10: HV polarization channel of Sentinel-1 image, SIT distribution from six SIT products (C3S-1, C3S-2, OSISAF-SIT, IFREMER-A, KNMI-A, and Zhang-SIT) and NSIDC-SIA, 3-daily ice drift, along with air temperature and sea surface wind from ECMWF ERA5 reanalysis on April 27, 2015.**

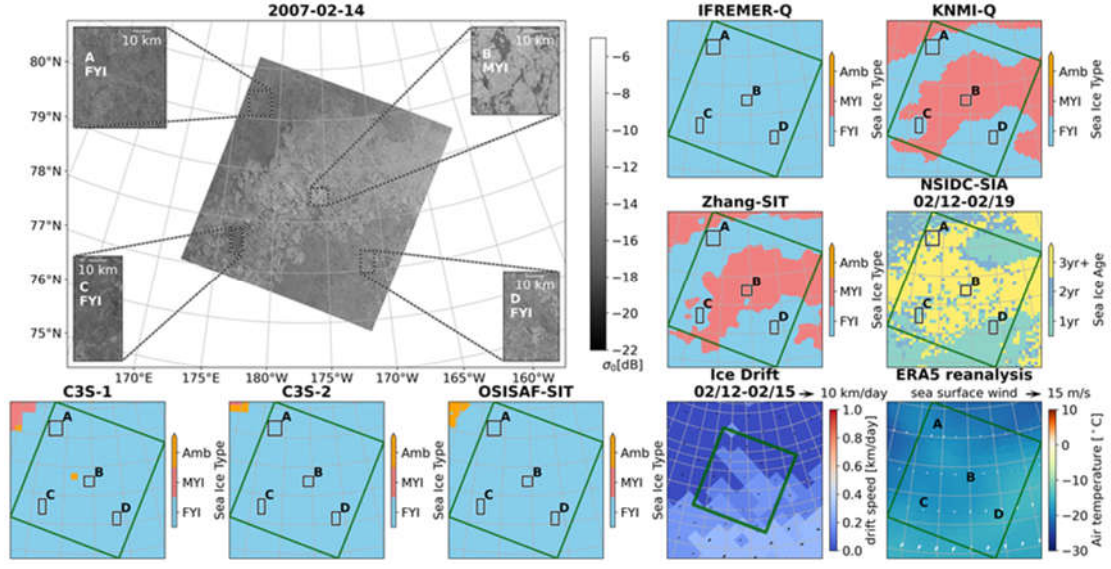

690 **Figure 11: RS-1 image, SIT distribution from six SIT products (C3S-1, C3S-2, OSISAF-SIT, IFREMER-A, KNMI-Q, and Zhang-SIT) and NSIDC-SIA, 3-daily ice drift, along with air temperature and sea surface wind from ECMWF ERA5 reanalysis on February 14, 2007.**

https://doi.org/10.5194/tc-2022-95
Preprint. Discussion started: 19 May 2022

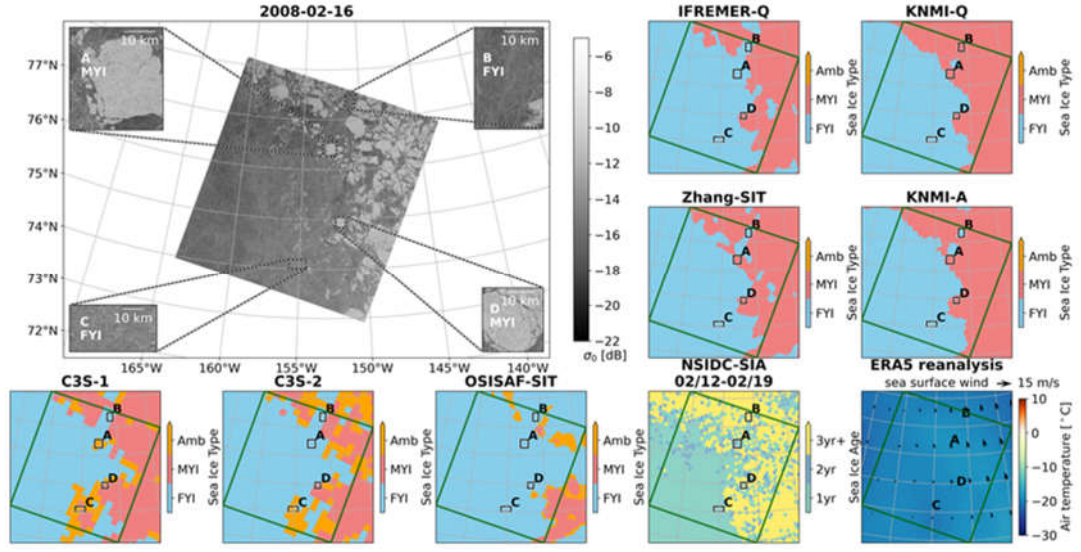

Figure 12: RS-1 image, SIT distribution from seven SIT products (C3S-1, C3S-2, OSISAF-SIT, IFREMER-Q, KNMI-Q, KNMI-A, and Zhang-SIT) and NSIDC-SIA, along with air temperature and sea surface wind from ECMWF ERA5 reanalysis on February 16, 2008.

Table 2. Performances of SIT and SIA products compared to SAR images

SIT products	Case 1	Case 2	Case 3	Case 4	Case 5
C3S-1	-	○	+-	--	+
C3S-2	-	○	+	--	+-
OSISAF-SIT	--	-	+-	--	--
KNMI-Q	+	/	/	○	+
KNMI-A	++	++	○	/	○
IFREMER-Q	-	/	/	--	-
IFREMER-A	/	/	--	/	/
Zhang-SIT	○	--	--	○	○
NSIDC-SIA	+	-	-	+-	+

○: best matches, +/-: overestimates/underestimates MYI, ++/--: overestimates/underestimates MYI in greater degree, /: no data.

Table 3. Satellite observations and methods used in the SIT retrieval methods

SIT retrieval methods	Input parameters		Classification method	Correction method
	Radiometer	Scatterometer		
C3S-1	GR_{37v19v}	\	dynamic PDF, Bayesian method	filters for open water*, geographical mask, 'extreme' value threshold filter
C3S-2	GR_{37v19v}	\	dynamic PDF, Bayesian method	filters for open water*, geographical mask, 'extreme' value threshold filter, temperature-based correction
OSISAF-SIT	GR_{19v37v}	σ^{0**}	dynamic PDF***, Bayesian method	geographical mask, 'extreme' value threshold filter
KNMI-SIT	\	σ^0	fixed thresholds	geographical mask
IFREMER-SIT	\	σ^0	thresholds moving in time	\

https://doi.org/10.5194/tc-2022-95
Preprint. Discussion started: 19 May 2022

Zhang-SIT	TB_{36h}	σ^0	adaptive clustering	ice motion confining and spatial filtering

* Climatological maximum extent, open water filter based on gradient ratio and temperature values are used to verify the discriminate between sea ice open water. In this study, discussion of correction methods focuses on those for MYI and FYI. ** Scatterometer data from ASCAT was introduced in 2009. *** Dynamical PDF based on daily training data was introduced in 2015.

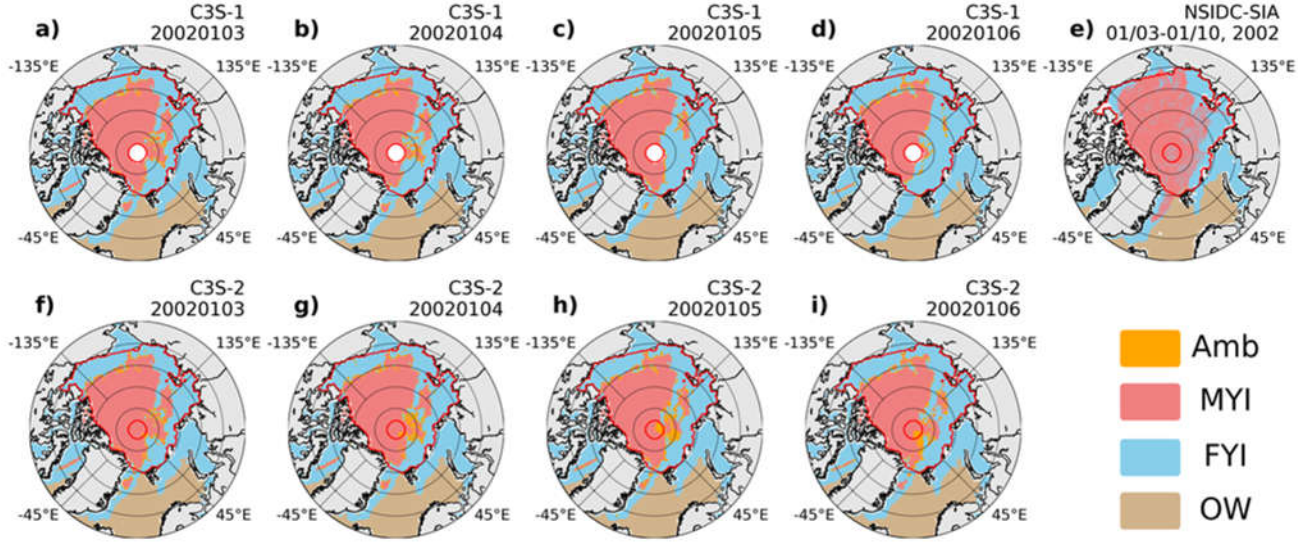

Figure. A1: Arctic SIT distribution maps from daily SIT product C3S-1 (a-d), C3S-2 (f-i) and weekly NSIDC-SIA product (g) from January 3 to January 6, 2002.

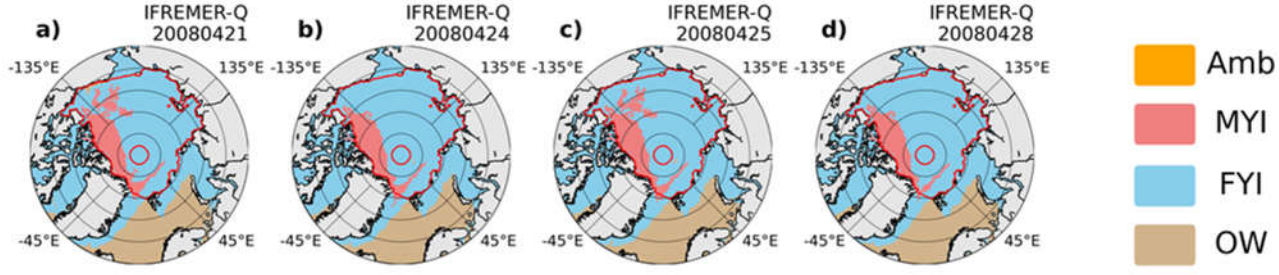

Figure. A2: Arctic SIT distribution maps from daily SIT product IFREMER-Q product (a-d) in April, 2008.